

Probing quadruplet scalar dark matter at current and future pp colliders

Yu-Pan Zeng, Chengfeng Cai, Dan-Yang Liu, Zhao-Huan Yu,^{*} and Hong-Hao Zhang[†]
School of Physics, Sun Yat-Sen University, Guangzhou 510275, China

We investigate a dark matter model involving an inert $SU(2)_L$ quadruplet scalar with hypercharge $1/2$. After the electroweak symmetry breaking, the dark sector contains one doubly charged, two singly charged, and two neutral scalars. The lighter neutral scalar can be a viable dark matter candidate. Electroweak production of these scalars at the Large Hadron Collider leads to potential signals in the monojet + \cancel{E}_T and soft-leptons + jets + \cancel{E}_T channels. We thus derive constraints on the model by reinterpreting recent experimental searches. Based on simulation, we further evaluate the sensitivity at a future 100 TeV pp collider.

^{*} yuzhaoh5@mail.sysu.edu.cn

[†] zhz98@mail.sysu.edu.cn

CONTENTS

I. Introduction	3
II. Quadruplet scalar dark matter model	4
III. Relic abundance and direct detection	7
IV. Monojet searches at pp colliders	9
A. LHC constraint	11
B. Sensitivity at a 100 TeV pp collider	13
V. Soft-lepton searches at pp colliders	15
A. LHC constraint	16
B. Sensitivity at a 100 TeV pp collider	18
VI. Conclusions and discussions	21
Acknowledgments	22
A. Electroweak gauge interactions of the quadruplet scalar	23
References	24

I. INTRODUCTION

Among various candidates of particle dark matter (DM), weakly interacting massive particles (WIMPs) seem rather appealing, because they could naturally predict a thermal relic abundance consistent with the observed value [1–3]. It is straightforward to construct WIMP models by extending the standard model (SM) with new colorless $SU(2)_L$ multiplets in the dark sector [4–33], which have electroweak interaction strength by definition. The DM candidate in such models arises from the electrically neutral components of the multiplets.

If the DM candidate is a scalar particle, the minimal extension is to introduce an inert $SU(2)_L$ doublet scalar with hypercharge $Y = 1/2$, resulting in the inert doublet model (IDM) [34–37]. The term “inert” means that there exists an unbroken Z_2 symmetry that forbids the doublet gaining a nonzero vacuum expectation value (VEV) and directly coupling to SM fermions. Consequently, if the lightest component of the doublet is one of the electrically neutral components, it would be stable, acting as a WIMP DM candidate. A next-to-minimal model can be constructed with an inert triplet scalar of $Y = 0$ or $Y = 1$ [38–42].

In this paper, we go further to study a scalar DM model with an inert quadruplet scalar of $Y = 1/2$ [10, 19], dubbed the quadruplet scalar dark matter (QSDM) model, which has been much less investigated in the past. The study in Ref. [10] focused on how this model can support a strong first-order electroweak phase transition, as well as the constraints from electroweak oblique parameters, invisible Higgs decay, direct DM detection, and relic abundance. In our previous work [19], we investigated the projected sensitivity to this model from improved determination of electroweak oblique parameters in the future Circular Electron-Positron Collider (CEPC) project [43]. In this work, we concentrate on production signals of the new scalar bosons in the model at the Large Hadron Collider (LHC) and future pp colliders, which have not been studied in the previous literature.

In the QSDM model, there are three types of independent quartic couplings between the quadruplet and the SM Higgs doublet, which contribute to the mass terms of the quadruplet components due to the nonzero Higgs VEV. As a result, the components of the quadruplet are split in mass. Mass eigenstates in the dark sector include two neutral scalars, two singly charged scalars, and one doubly charged scalar. The lighter neutral scalar could be a viable DM candidate. DM scattering off nuclei can be mediated by the Higgs boson through the quartic couplings, leading to possible signals in direct detection experiments.

Moreover, the dark sector scalars could be produced in pairs at the LHC via electroweak gauge interactions. Because of the Z_2 symmetry, all these scalars finally decay into the DM particle, which can escape from the LHC detectors, resulting in a large missing transverse energy (\cancel{E}_T) in the final state. Since the mass spectrum in the dark sector is typically compressed, visible decay products from the scalars tend to be soft. Therefore, a hard jet from initial state radiation may be required for triggering the signal at the LHC. Thus, one possible searching channel is the monojet + \cancel{E}_T channel, which has been widely applied for

searching dark matter [44–49]. Furthermore, additional soft leptons may contain imprints of the scalar decays [50–54]. This motivates us to study a soft-leptons + jets + \cancel{E}_T channel as well. We will estimate the related constraints on the QSDM model by reinterpreting the existed LHC searches.

At the LHC energies, electroweak production rates for the dark sector scalars are quite low, and, hence, the constraints from current LHC searches are still weak. Nevertheless, future pp colliders with much higher energies have been proposed, including the Super Proton-Proton Collider (SPPC) at $\sqrt{s} \sim 70\text{--}100$ TeV [55] and the pp Future Circular Collider (FCC-hh) at $\sqrt{s} \sim 100$ TeV [56]. The increase of the collision energy makes it possible to probe much heavier electroweak scalars. We thus explore the sensitivity to the QSDM model at a 100 TeV pp collider based on Monte Carlo simulation.

This paper is organized as follows. In Sec. II, we introduce the model details. In Sec. III, we identify the parameter regions that are consistent with the observed relic abundance and study the constraints from direct detection experiments. In Sec. IV, we explore the constraint from the LHC search in the monojet + \cancel{E}_T channel, as well as the sensitivity at a 100 TeV pp collider. In Sec. V, the soft-leptons + jets + \cancel{E}_T channel is studied. Section VI gives the conclusions and discussions.

II. QUADRUPLLET SCALAR DARK MATTER MODEL

In the QSDM model, we introduce a $SU(2)_L$ quadruplet scalar X with hypercharge $Y = 1/2$ [10, 19]. We assume that X is inert; i.e., X is odd under a Z_2 symmetry, but all SM fields are Z_2 even. On the one hand, we can express the quadruplet in the vector notation $X = (X^{++}, X^+, X^0, X^-)^T$ with explicitly indicated electric charges. On the other hand, it can be denoted by a totally symmetric $SU(2)_L$ tensor X^{ijk} ($i, j, k = 1, 2$). The components in the two notations are related by

$$X = \begin{pmatrix} X^{++} \\ X^+ \\ X^0 \\ X^- \end{pmatrix} = \begin{pmatrix} X^{111} \\ \sqrt{3}X^{112} \\ \sqrt{3}X^{122} \\ X^{222} \end{pmatrix}. \quad (1)$$

Note that $X^+ \neq (X^-)^*$. The neutral component X^0 can be separated into two real scalars ϕ and a :

$$X^0 = \frac{1}{\sqrt{2}}(\phi + ia). \quad (2)$$

The Lagrangian in the QSDM model is given by

$$\mathcal{L} = \mathcal{L}_{\text{SM}} + (D_\mu X)^\dagger D^\mu X - V(X), \quad (3)$$

where \mathcal{L}_{SM} is the SM Lagrangian and $V(X)$ is the potential involving X . The covariant derivative for X is $D_\mu = \partial_\mu - igW_\mu^a T^a - ig'B_\mu/2$, where T^a are the $\text{SU}(2)_L$ generators in the representation **4**. Electroweak gauge interaction terms for the quadruplet are explicitly given in Appendix A.

Respecting the Z_2 symmetry $X^{ijk} \rightarrow -X^{ijk}$, we write down the potential $V(X)$ as

$$V(X) = M_X^2 |X|^2 + \lambda_0 |X|^2 |H|^2 + \lambda_1 X_{ijk}^\dagger X^{ijl} H_l^\dagger H^k + (\lambda_2 X^{ikl} X^{jmn} H_i^\dagger H_j^\dagger \epsilon_{km} \epsilon_{ln} + \text{H.c.}) + \text{self-interaction terms of } X, \quad (4)$$

where H is the SM Higgs doublet. Here we adopt a convention $\epsilon^{12} = 1 = -\epsilon_{12}$ for the asymmetric tensors ϵ^{ij} and ϵ_{ij} . We do not give the explicit forms for the quadruplet self-interaction terms, because they will not affect the following discussions. Note that one may write down an extra operator $X_{ijk}^\dagger X^{ijl} H_m^\dagger H^n \epsilon^{km} \epsilon_{ln}$, but it is not independent, because $X_{ijk}^\dagger X^{ijl} H_m^\dagger H^n \epsilon^{km} \epsilon_{ln} = X_{ijk}^\dagger X^{ijl} H_l^\dagger H^k - |X|^2 |H|^2$. If λ_2 is complex, we can always make it real by a phase redefinition of the quadruplet. Hereafter, we just use a real λ_2 . Since the one-loop contributions to the beta function of the quartic Higgs coupling λ from λ_0 , λ_1 , and λ_2 are all positive [57], the Higgs vacuum stability problem in the SM [58] would be partially alleviated in the QSDM model.

After H gets its VEV $v = 246.22$ GeV, mass terms for the quadruplet components can be expressed as

$$\mathcal{L}_{\text{mass}} = -\frac{1}{2} m_\phi^2 \phi^2 - \frac{1}{2} m_a^2 a^2 - \left((X^+)^* \ X^- \right) M_C^2 \begin{pmatrix} X^+ \\ (X^-)^* \end{pmatrix} - m_{++}^2 |X^{++}|^2, \quad (5)$$

with

$$m_\phi^2 = M_X^2 + \frac{1}{6} (3\lambda_0 + 2\lambda_1 - 4\lambda_2) v^2, \quad (6)$$

$$m_a^2 = M_X^2 + \frac{1}{6} (3\lambda_0 + 2\lambda_1 + 4\lambda_2) v^2, \quad (7)$$

$$M_C^2 = \begin{pmatrix} M_X^2 + (3\lambda_0 + \lambda_1) v^2 / 6 & \lambda_2 v^2 / \sqrt{3} \\ \lambda_2 v^2 / \sqrt{3} & M_X^2 + (\lambda_0 + \lambda_1) v^2 / 2 \end{pmatrix}, \quad (8)$$

$$m_{++}^2 = M_X^2 + \frac{1}{2} \lambda_0 v^2. \quad (9)$$

The mass-squared matrix M_C^2 for the singly charged scalars can be diagonalized by a 2×2 rotation matrix O , which satisfies

$$O^T M_C^2 O = \begin{pmatrix} m_1^2 & \\ & m_2^2 \end{pmatrix}, \quad (10)$$

$$O = \begin{pmatrix} \cos \theta & -\sin \theta \\ \sin \theta & \cos \theta \end{pmatrix}. \quad (11)$$

The rotation angel θ can be obtained from

$$\sin \theta = \frac{-\sqrt{6}\lambda_2}{\sqrt{\lambda_1^2 + 12\lambda_2^2 + \lambda_1\sqrt{\lambda_1^2 + 12\lambda_2^2}}}. \quad (12)$$

Thus, the singly charged mass eigenstates X_1^+ and X_2^+ are related to the gauge eigenstates X^+ and $(X^-)^*$ through

$$\begin{pmatrix} X^+ \\ (X^-)^* \end{pmatrix} = O \begin{pmatrix} X_1^+ \\ X_2^+ \end{pmatrix}. \quad (13)$$

Their masses squared are given by

$$m_1^2 = M_X^2 + \frac{v^2}{12} \left(6\lambda_0 + 4\lambda_1 - 2\sqrt{\lambda_1^2 + 12\lambda_2^2} \right), \quad (14)$$

$$m_2^2 = M_X^2 + \frac{v^2}{12} \left(6\lambda_0 + 4\lambda_1 + 2\sqrt{\lambda_1^2 + 12\lambda_2^2} \right). \quad (15)$$

The mass hierarchy of the neutral scalars ϕ and a is determined by the sign of λ_2 . If $\lambda_2 > 0$ ($\lambda_2 < 0$), ϕ is lighter (heavier) than a , and, thus, ϕ (a) is a possible DM candidate. Nevertheless, if $|\lambda_1| > 2|\lambda_2|$, one of the singly charged scalars is lighter than the DM candidate. Additionally, if $\lambda_1 > 2|\lambda_2|$, the doubly charged scalar is lighter than the DM candidate. Since the DM candidate should be the lightest particle in the dark sector for ensuring its stability, we have the following conclusions.

- If $\lambda_2 > 0$ and $|\lambda_1| \leq 2\lambda_2$, then ϕ is a viable DM candidate.
- If $\lambda_2 < 0$ and $|\lambda_1| \leq -2\lambda_2$, then a is a viable DM candidate.

Similar to the IDM, the QSDM model has two kinds of CP symmetries, one with $\phi \rightarrow \phi$ and $a \rightarrow -a$ and the other one with $\phi \rightarrow -\phi$ and $a \rightarrow a$ [59]. A transformation $X^{ijk} \rightarrow iX^{ijk}$ and $\lambda_2 \rightarrow -\lambda_2$ can keep the Lagrangian unchanged but interchange the two CP symmetries and, hence, the roles of ϕ and a . Therefore, we know that ϕ and a have opposite CP parities, but it is impossible to determine their absolute CP parities without additional interactions. Without loss of generality, hereafter we adopt $\lambda_2 > 0$ and take ϕ as the DM candidate. The resulting discussions are totally equivalent to those for $\lambda_2 < 0$ and a as the DM candidate.

In the following analyses, four free parameters in the QSDM model are chosen to be $\{M_X, \lambda_0, \lambda_1, \lambda_2\}$. The parameter space is analogous to that of the IDM (cf. Refs. [35–37, 59]) in the sense of the number and the roles of the parameters. Nonetheless, the number of dark sector scalars in the QSDM model is more. The IDM dark sector includes two neutral scalars with opposite CP and one singly charged scalar. The neutral scalars in the two models play similar roles, with the lighter one being the DM candidate. On the other hand, the QSDM model contains one more singly charged scalar and an additional doubly charged scalar. After electroweak symmetry breaking, the mass eigenstates of singly

charged scalars are different from the gauge eigenstates. This is a new phenomenon that does not exhibit in the IDM.

III. RELIC ABUNDANCE AND DIRECT DETECTION

In this section, we evaluate the relic abundance prediction in the QSDM model, and investigate the constraints from direct detection experiments.

The dark sector scalars can interact with SM particles via electroweak gauge couplings and scalar couplings to the Higgs boson. Through such interactions, these scalars could be thermally produced in the early Universe and decoupled from the cosmic plasma at the freeze-out epoch. Conventionally, the relic abundance of dark matter is determined by its freeze-out annihilation cross section. Nonetheless, for $m_X \sim \mathcal{O}(\text{TeV})$, the mass splittings among the dark sector scalars due to the quartic couplings would be relatively small, and, thus, the scalars actually freeze out around the same epoch. Therefore, the coannihilation effect would be significant for evaluating the relic abundance [60].

There are a lot of relevant annihilation and coannihilation processes. For instance, a $\phi\phi$ pair can annihilate into a SM fermion pair $f\bar{f}$, or an electroweak gauge boson pair W^+W^- or ZZ , or a Higgs boson pair hh . Some of these annihilation processes are mediated by s -channel Z and Higgs bosons, while the others are related to the exchanges of t - and u -channel dark sector scalars as well as to the quartic couplings. Because of the significant coannihilation effect, it is not sufficient to just consider the processes that are directly related to DM annihilation. Actually, annihilation or coannihilation between every pair of dark sector scalars could affect the final DM relic abundance.

We utilize a few numerical tools to predict the relic abundance of the DM candidate ϕ . **FeynRules 2** [61] is adopted to implement the QSDM model, interfaced to the Monte Carlo generator **MadGraph5_aMC@NLO 2** [62]. The relic abundance $\Omega_\phi h^2$ is calculated by a **MadGraph** plugin **MadDM** [63], which can reliably take into account the coannihilation effect. All annihilation and coannihilation diagrams are automatically involved in the calculation.

The measurement of the DM relic abundance in the Planck experiment gives $\Omega_{\text{DM}} = 0.1200 \pm 0.0012$ [64]. In Figs. 1(a) and 1(b), we fix the parameters $(\lambda_0, \lambda_1) = (0.5, 0.05)$ and $(\lambda_0, \lambda_2) = (0.7, 0.5)$ and show the parameter regions that are consistent with the Planck observation as the blue bands in the M_X - λ_2 and M_X - λ_1 planes, respectively. The black dotted lines indicate the contours of the DM candidate mass m_ϕ , which slightly deviates from M_X due to the quartic couplings.

If M_X increases, the effective annihilation cross section typically decreases, leading to an increase in the relic abundance. Therefore, the light blue regions with large M_X predict overproduction of ϕ particles in the early Universe, which contradicts standard cosmology. For small values of λ_2 ($|\lambda_1|$) in Fig. 1(a) [Fig. 1(b)], the relic abundance observation corresponds to $M_X \sim 2.4$ (3.3) TeV, which increases to $M_X \sim 5$ (4.6) TeV when λ_2 ($|\lambda_1|$) increases to

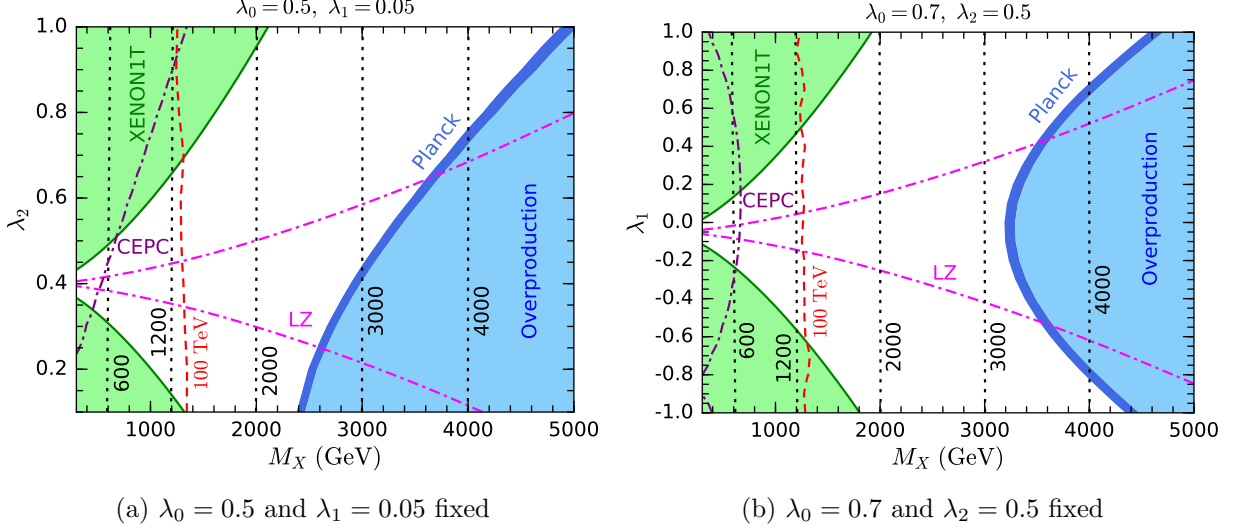


FIG. 1. Experimental constraints and sensitivities in the M_X - λ_2 (a) and M_X - λ_1 (b) planes. The black dotted lines denote the DM candidate mass m_ϕ in GeV. The blue bands correspond to the 3σ range of the Planck relic abundance measurement [64], while the light blue regions predict overproduction of dark matter. The green regions are excluded by the direct detection experiment XENON1T [65]. The dot-dashed magenta lines indicate the exclusion capability of the future direct detect experiment LZ [66]. The dot-dashed purple lines show the expected sensitivities of the measurement of electroweak oblique parameters at the future CEPC. The dashed red lines show the exclusion capability of the monojet + \cancel{E}_T channel at a 100 TeV pp collider with a dataset of 3 ab^{-1} (see Sec. IV).

one. These results are consistent with the simplified calculation given in Ref. [5].

Direct detection experiments look for signals of DM scattering off nuclei. In the QSDM model, DM scattering is mediated by the Higgs boson h , arising from the quartic potential terms that lead to the $h\phi\phi$ interaction Lagrangian

$$\mathcal{L}_{h\phi\phi} = \frac{1}{2}\lambda_{h\phi\phi}vh\phi^2, \quad (16)$$

$$\lambda_{h\phi\phi} = -\lambda_0 - \frac{2}{3}\lambda_1 + \frac{4}{3}\lambda_2. \quad (17)$$

As direct detection experiments basically operate at zero momentum transfer, the interactions between DM and quarks can be described by dimension-5 effective operators [67]. As a result, the spin-independent DM-nucleon scattering cross section can be expressed as

$$\sigma_{\chi N}^{\text{SI}} = \frac{m_N^2 F_N^2}{4\pi(m_\phi + m_N)^2}, \quad N = p, n, \quad (18)$$

where

$$F_N = -\frac{\lambda_{h\phi\phi}m_N}{9m_h^2}[2 + 7(f_u^N + f_d^N + f_s^N)]. \quad (19)$$

Here the nucleon form factors f_q^N are given by [68]

$$\begin{aligned} f_u^p &= 0.020 \pm 0.004, & f_d^p &= 0.026 \pm 0.005, & f_u^n &= 0.014 \pm 0.003, \\ f_d^n &= 0.036 \pm 0.008, & f_s^p &= f_s^n = 0.118 \pm 0.062. \end{aligned} \quad (20)$$

In Figs. 1(a) and 1(b), we show the parameter regions excluded by the direct detection experiment XENON1T [65] at 90% confidence level (C.L.). According to Eq. (17), we can take some particular relations among λ_0 , λ_1 , and λ_2 to give a vanishing $h\phi\phi$ coupling, resulting in “blind spots” for direct detection experiments. These relations correspond to the flat directions among the scalar couplings, where the Higgs VEV has zero contribution to m_ϕ . For Figs. 1(a) and 1(b), the limits $\lambda_2 = 3\lambda_0/4 + \lambda_1/2 = 0.4$ and $\lambda_1 = -3\lambda_0/2 + 2\lambda_2 = -0.05$ correspond to $\lambda_{h\phi\phi} = 0$, respectively. Therefore, direct detection experiments lose their sensitivities as λ_2 or λ_1 approaches the corresponding limit. Nonetheless, the XENON1T experiment has excluded some disconnected parameter regions with $M_X \lesssim 1.3\text{--}2$ TeV. We also demonstrate the expected 90% C.L. exclusion limits of the future direct detection experiment LZ [66], which will explore the parameter space much deeper and be able to reach the regions suggested by the relic abundance measurement.

Note that the results presented here are based on tree-level calculations. There are also contributions from electroweak loop-induced diagrams [5, 12], leading to a nonvanishing spin-independent cross section for the tree-level blind spots. Nevertheless, one would expect a cancellation between the tree and loop diagrams if the scalar couplings are carefully tuned. This means that the blind spots would still exist at loop level, but their positions in the parameter space would be slightly shifted.

As studied in previous papers [10, 19], the dark sector scalars in the QSDM model can contribute to the electroweak oblique parameters S , T , and U at one-loop level, and, hence, affect electroweak precision measurements. In Fig. 1, we also show the 95% C.L. expected sensitivities of the measurement of electroweak oblique parameters at the future CEPC project [43]. This result is estimated following the strategy in our previous work [19] with the optimistic settings. We can see that the CEPC experiment would probe up to $m_X \sim 600\text{--}1200$ GeV, covering some regions related to the blind spots in direct detection.

IV. MONOJET SEARCHES AT pp COLLIDERS

Through the electroweak gauge couplings, the dark sector scalars in the QSDM model could be directly produced in pairs at the LHC. The corresponding processes can be expressed as $pp \rightarrow \chi_i \chi_j + \text{jets}$ with $\chi_i = (\phi, a, X_1^\pm, X_2^\pm, X^{\pm\pm})$. Figure 2 shows some typical parton-level diagrams for pair production of dark sector scalars at the LHC. After production, a heavier scalar χ_k may decay into a lighter scalar χ_l via $\chi_k \rightarrow W^{\pm(*)}/Z^{(*)}/h^{(*)} + \chi_l$. Typical decay diagrams are demonstrated in Fig. 3. Depending on the mass splitting between χ_k and χ_l , the produced W^\pm , Z , and h bosons can be either on or off shell. Subsequent

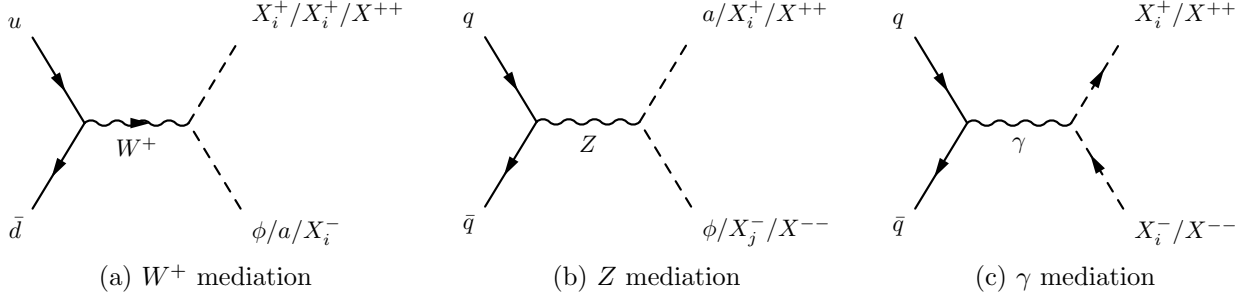


FIG. 2. Typical diagrams for pair production of dark sector scalars at parton level in pp collisions, including W^+ -mediated $u + \bar{d} \rightarrow X_i^+/X_i^+/X^{++} + \phi/a/X_i^-$ (a), Z -mediated $q + \bar{q} \rightarrow a/X_i^+/X^{++} + \phi/X_j^-/X^{--}$ (b), and γ -mediated $q + \bar{q} \rightarrow X_i^+/X^{++} + X_i^-/X^{--}$ (c).

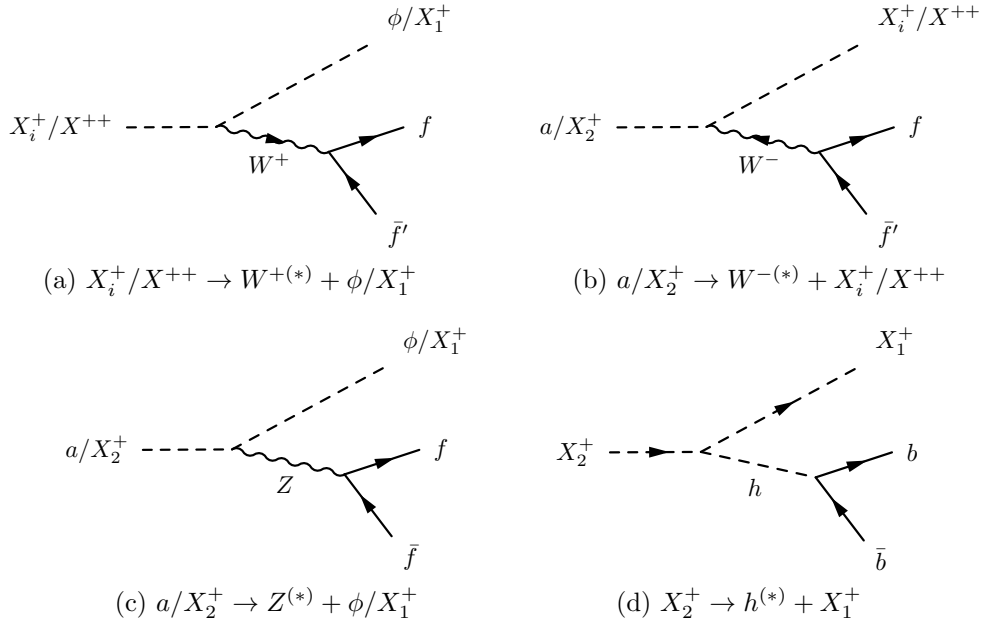


FIG. 3. Typical decay diagrams for dark sector scalars, including $X_i^+/X^{++} \rightarrow W^{+(*)} + \phi/X_1^+$ (a), $a/X_2^+ \rightarrow W^{-(*)} + X_i^+/X^{++}$ (b), $a/X_2^+ \rightarrow Z^{(*)} + \phi/X_1^+$ (c), and $X_2^+ \rightarrow h^{(*)} + X_1^+$ (d).

decays may happen and form decay chains. Finally, all Z_2 -odd scalars will decay into the DM candidate ϕ , which is stable and escapes from detection, leading to a large \cancel{E}_T .

Figure 4 shows the mass splittings between $(a, X_1^\pm, X_2^\pm, X^{\pm\pm})$ and ϕ as functions of M_X for $\lambda_0 = 0.1$ and $\lambda_1 = \lambda_2 = 0.2$. From this plot, we can read off the mass difference between each pair of dark sector scalars. As M_X increases, the contributions from the quartic couplings relatively decrease, resulting in smaller splittings. The mass splitting between the two neutral scalars a and ϕ is the largest one, ranging from ~ 100 to ~ 2 GeV as m_X increases from 40 GeV to 5 TeV. For $m_X \gtrsim 70$ GeV, the splittings are not large enough to induce on-shell W^\pm , Z , or h bosons. For fixed M_X , smaller quartic couplings would further compress the mass spectrum.

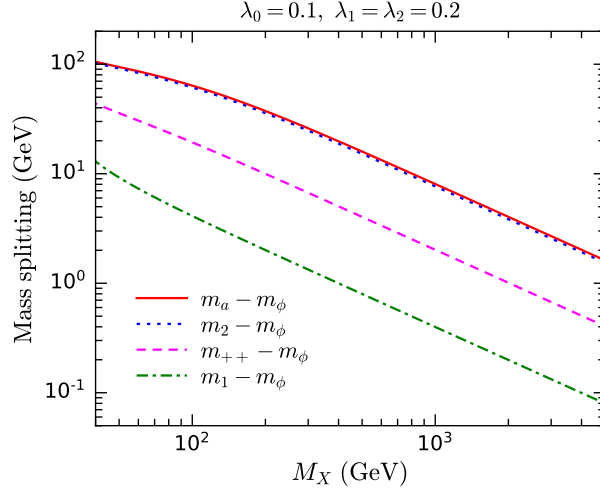


FIG. 4. Mass splittings as functions of M_X for $\lambda_0 = 0.1$ and $\lambda_1 = \lambda_2 = 0.2$.

In the above analysis, we find that the mass splittings in the QSDM model are typically small. Consequently, visible decay products from the dark sector scalars would be quite soft and, hence, difficult to be triggered in detectors. In order to effectively trigger the signal, we can require at least one hard jet from initial state radiation to recoil the $\chi_i\chi_j$ pair, leading to a monojet + \cancel{E}_T final state [44–46]. SM backgrounds in the monojet + \cancel{E}_T search channel include two major backgrounds— $W(\rightarrow l\nu) + \text{jets}$ and $Z(\rightarrow \nu\bar{\nu}) + \text{jets}$ —and some minor backgrounds, such as $t\bar{t} + \text{jets}$ and $VV + \text{jets}$ ($V = W^\pm, Z$). In these backgrounds, \cancel{E}_T mainly arises from neutrinos in the decay products.

A. LHC constraint

In this subsection, we investigate the current LHC constraint on the QSDM model by reinterpreting the ATLAS analysis in the monojet + \cancel{E}_T channel with an integrated luminosity of 36.1 fb^{-1} at $\sqrt{s} = 13 \text{ TeV}$ [69]. For this purpose, we utilize **MadGraph** [62] to generate signal simulation samples. Parton shower is performed by **PYTHIA 8** [70] with the MLM matching scheme [71]. **PYTHIA** is also carried out for hadronization and decay processes. Then we use **Delphes 3** [72] for a fast detector simulation with a setup for the ATLAS detector.

We simulate the signal processes $pp \rightarrow \chi_i\chi_j + \text{jets}$ and apply the same selection cuts in the ATLAS analysis [69] to the simulation events. Isolated leptons, including electrons and muons, and jets are reconstructed with the conditions on p_T and η listed in Table I. Then the events in the signal regions are required to have a hard leading jet with $p_T > 250 \text{ GeV}$ and $|\eta| < 2.4$ and a missing transverse energy \cancel{E}_T at least larger than 250 GeV. In addition, there should be no leptons and no more than four jets. Moreover, the separation in the azimuthal angle between any reconstructed jet j_i and the missing transverse momentum \cancel{p}_T should

TABLE I. Reconstruction and cut conditions in the monojet + \cancel{E}_T channel.

	13 TeV LHC	100 TeV pp collider
Reconstruction conditions		
Electron $p_T, \eta $	$> 20 \text{ GeV}, < 2.47$	$> 40 \text{ GeV}, < 2.47$
Muon $p_T, \eta $	$> 10 \text{ GeV}, < 2.5$	$> 20 \text{ GeV}, < 2.5$
Jet $p_T, \eta $	$> 30 \text{ GeV}, < 2.8$	$> 60 \text{ GeV}, < 2.8$
Cut conditions		
Number of leptons	0	0
Leading jet $p_T, \eta $	$> 250 \text{ GeV}, < 2.4$	$> 1.4 \text{ TeV}, < 2.4$
Number of jets	≤ 4	≤ 4
$\Delta\phi(j_i, \mathbf{p}_T)$	> 0.4	> 0.4
\cancel{E}_T	$> 250\text{--}1000 \text{ GeV}$	$> 1.5\text{--}2.8 \text{ TeV}$

satisfy $\Delta\phi(j_i, \mathbf{p}_T) > 0.4$ for preventing a large \cancel{E}_T from mismeasurement of jets. Finally, ten inclusive and ten exclusive signal regions are defined with different \cancel{E}_T thresholds, whose explicit definitions can be found in Table 1 of Ref. [69]. In Table I, we summarize the cut conditions above.

Based on the signal simulation samples, we estimate the visible cross section in each signal region, which is a product of production cross section, acceptance, and efficiency, and then use the 95% C.L. observed experimental upper limit to derive constraints on the QSDM model. Taking into account all the signal regions, the combined exclusion region in the m_ϕ - λ_2 plane is shown in Fig. 5(a), where we fix a coupling relation of $\lambda_1 = \lambda_2 = 3\lambda_0/2$. Because of Eq. (17), such a relation leads to $\lambda_{h\phi\phi} = 0$, and there is no constraint from direct detection experiments. Therefore, collider searches are really important in this case. Note that $\lambda_{h\phi\phi} = 0$ also leads to $m_\phi = m_X$, according to Eqs. (6) and (17). We find that the monojet search has excluded a region with $m_\phi \lesssim 33 \text{ GeV}$ and $\lambda_2 \lesssim 0.3$. Nonetheless, the sensitivity decreases as λ_2 increases. The reason is that a larger λ_2 leads to larger mass splittings among the dark sector scalars and, hence, harder leptons from scalar decays that would not be easy to pass the cuts.

In Fig. 5(b), we adopt another relation $\lambda_0 = 0$ and $\lambda_1 = 2\lambda_2$, which also results in $\lambda_{h\phi\phi} = 0$. Additionally, it leads to degenerate mass spectra with $m_\phi = m_1 = m_{++}$ and $m_a = m_2$. Consequently, many decay channels are turned off, significantly reducing the probability of finding leptons in the final state. Therefore, the monojet search is more sensitive, excluding a region up to $m_\phi \sim 45 \text{ GeV}$. The exclusion is basically regardless of the λ_2 value.

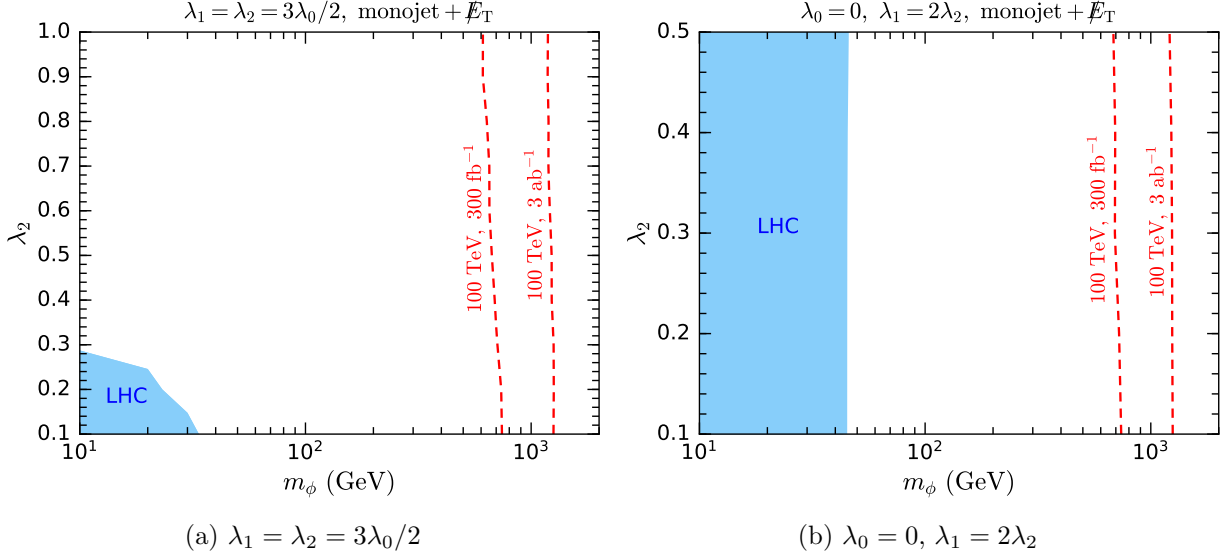


FIG. 5. Current constraints and future sensitivities from the monojet + \cancel{E}_T channel in the m_ϕ - λ_2 plane for the fixed coupling relations of $\lambda_1 = \lambda_2 = 3\lambda_0/2$ (a) and of $\lambda_0 = 0$ and $\lambda_1 = 2\lambda_2$ (b). The blue regions are excluded at 95% C.L. by the ATLAS search with a 36.1 fb^{-1} dataset at the 13 TeV LHC [69]. The red dashed lines denote the 95% C.L. expected exclusion limits at a 100 TeV pp collider with integrated luminosities of 300 fb^{-1} and 3 ab^{-1} .

B. Sensitivity at a 100 TeV pp collider

The above results have shown that the current LHC monojet search is rather insensitive to the QSDM model, just probing a scale of a few tens of GeV. Since production cross sections in pp collisions typically increase as \sqrt{s} increases, we expect that monojet searches at a future pp collider with $\sqrt{s} \sim 100 \text{ TeV}$ would be much more sensitive. Below we estimate the projected sensitivity in the monojet + \cancel{E}_T channel at a 100 TeV pp collider based on simulation. The obtained results would be applicable to both the SPCC and FCC-hh projects.

In the simulation with $\sqrt{s} = 100 \text{ TeV}$, we consider the signal processes and only the primary SM backgrounds $W(\rightarrow \ell\nu) + \text{jets}$ and $Z(\rightarrow \nu\bar{\nu}) + \text{jets}$. Other backgrounds should be small and can be safely neglected. In the `Delphes` simulation, we conservatively assume that the future detector has the same parameters as those in the ATLAS detector. The thresholds in the reconstruction and cut conditions are appropriately adjusted for a 100 TeV pp collider, as also demonstrated in Table I.

Four signal regions are defined by requiring $\cancel{E}_T > 1.5, 1.8, 2.2, 2.8 \text{ TeV}$. In each signal region, the signal significance \mathcal{S} is defined as

$$\mathcal{S} = \frac{S}{\sqrt{S+B}}, \quad (21)$$

TABLE II. Information of the four benchmark points with the fixed coupling relation $\lambda_1 = \lambda_2 = 3\lambda_0/2$ for the monojet + \cancel{E}_T channel.

	M_X/GeV	λ_2	m_{++}/GeV	m_ϕ/GeV	m_a/GeV	m_1/GeV	m_2/GeV
BMP-a	400	0.2	405.0	400	419.7	401.0	418.7
BMP-b	700	0.2	702.9	700	711.4	700.6	710.9
BMP-c	1000	0.2	1002.0	1000	1008.0	1000.4	1007.6
BMP-d	1300	0.2	1301.6	1300	1306.2	1300.3	1305.9

TABLE III. Visible cross section σ_{vis} in femtobarns and signal significance \mathcal{S} for integrated luminosity 3 ab^{-1} after each cut in the signal region with $\cancel{E}_T > 1.5 \text{ TeV}$ of the monojet + \cancel{E}_T channel at $\sqrt{s} = 100 \text{ TeV}$.

	$W \rightarrow \ell\nu$	$Z \rightarrow \nu\bar{\nu}$	BMP-a		BMP-b		BMP-c		BMP-d	
	σ_{vis}	σ_{vis}	σ_{vis}	\mathcal{S}	σ_{vis}	\mathcal{S}	σ_{vis}	\mathcal{S}	σ_{vis}	\mathcal{S}
Cut 1	6080	1481	8.08	5.08	3.16	1.99	1.41	0.89	0.73	0.46
Cut 2	4428	1481	7.79	5.54	3.11	2.21	1.41	1.00	0.73	0.52
Cut 3	1442	654	5.24	6.26	2.32	2.77	1.07	1.27	0.56	0.66
Cut 4	62.7	139	3.65	13.8	1.80	6.81	0.87	3.31	0.47	1.79

where S and B are the estimated numbers of the signal events and the total background events passing the corresponding cuts, respectively.

In order to show the cut efficiency in the monojet + \cancel{E}_T channel, we adopt four benchmark points (BMPs) for the QSDM model, whose parameters and mass spectra are listed in Table II. All of them satisfy $\lambda_1 = \lambda_2 = 3\lambda/2$, leading to vanishing $h\phi\phi$ coupling and $m_\phi = m_X$. Thus, they would not be constrained by direct detection. We choose the same λ_2 but different m_X for the four BMPs. As discussed above, a larger m_X leads to a more compressed mass spectrum. The predicted relic abundances of these BMPs are lower than the observed value.

For the signal region with $\cancel{E}_T > 1.5 \text{ TeV}$, we divide the cut conditions into the following four cuts.

- *Cut 1.*—At least one reconstructed jet, and the leading jet with $p_T > 1.4 \text{ TeV}$ and $|\eta| < 2.4$.
- *Cut 2.*—No reconstructed lepton.
- *Cut 3.*—At most four reconstructed jets, and $\Delta\phi(j_i, \cancel{p}_T) > 0.4$.
- *Cut 4.*— $\cancel{E}_T > 1.5 \text{ TeV}$.

After applying the cuts one by one, the visible cross section σ_{vis} and the signal significance \mathcal{S} for an integrated luminosity of 3 ab^{-1} are tabulated in Table III. While cut 2 does not

affect the $Z(\rightarrow \nu\bar{\nu}) + \text{jets}$ background, it reduces the $W(\rightarrow \ell\nu) + \text{jets}$ background which has a genuine lepton in the final state. Cut 3 and cut 4 combined suppress the $W(\rightarrow \ell\nu) + \text{jets}$ [$Z(\rightarrow \nu\bar{\nu}) + \text{jets}$] background by 2 (1) orders of magnitude. For all the BMPs, these cuts subsequently increase the signal significance. Note that Eq. (21) does not take into account systematic uncertainties, which could be a few to ten percent in monojet searches. If systematic uncertainties are considered, the signal significance would be reduced. Since BMP-b, -c, and -d have a S/B ratio below 1%, it could be difficult to test them in this signal region.

Combining the four signal regions, the expected exclusion limits at 95% C.L. are shown in Figs. 5(a) and 5(b). For datasets of 300 fb^{-1} and 3 ab^{-1} at $\sqrt{s} = 100 \text{ TeV}$, monojet searches are expected to probe the DM candidate mass m_ϕ up to $\sim 700 \text{ GeV}$ and $\sim 1.2 \text{ TeV}$, respectively. Thus, a 100 TeV pp collider looks much more powerful than the LHC.

In order to compare with direct detection and relic abundance observation, we have also plotted the 95% C.L. expected exclusion limits in the monojet + \cancel{E}_T channel at $\sqrt{s} = 100 \text{ TeV}$ with an integrated luminosity of 3 ab^{-1} in Figs. 1(a) and 1(b). We find that the 100 TeV monojet searches could cover some regions where direct detection experiments cannot probe. Nonetheless, the regions predicting an observed relic abundance could not be reached.

V. SOFT-LEPTON SEARCHES AT pp COLLIDERS

Besides the monojet channel, leptons arising from the scalar decays $\chi_i \rightarrow \chi_j + W^{\pm(*)}(\rightarrow \ell^\pm \nu_\ell)/Z^{(*)}(\rightarrow \ell^\pm \ell^\mp)$ may also contain important information for exploring the QSMD model. Inspired by the searches for electroweak production of charginos and neutralinos in supersymmetric models, we first consider the final states involving two or three “hard” leptons. After recasting the related ATLAS analysis at $\sqrt{s} = 13 \text{ TeV}$ with a dataset of 36.1 fb^{-1} [73], however, we do not find any meaningful constraint on the QSMD model. The main reason is that the leptons from the scalar decays tend to be rather soft, because the mass spectrum is typically compressed, as explained in the previous section.

Therefore, it is more suitable to consider the final states with “soft” leptons. In this case, a pair of same-flavor opposite-sign (SFOS) soft leptons with an invariant mass $\lesssim 60 \text{ GeV}$ could lead to a distinct signature [53, 54]. In the signal process $pp \rightarrow \chi_i \chi_j + \text{jets}$, such a SFOS lepton pair may come from the scalar decays into an off-shell Z boson. In order to induce a sufficiently large \cancel{E}_T , a hard jet with a transverse direction roughly opposite to that of \vec{p}_T is also required. Such a soft-leptons + jets + \cancel{E}_T channel has been utilized in the ATLAS search for supersymmetric particles with compressed mass spectra at the 13 TeV LHC with an integrated luminosity of 36.1 fb^{-1} [74]. Important SM backgrounds in this channel include $t\bar{t} + \text{jets}$, $tW + \text{jets}$, $VV + \text{jets}$, and $\tau^+ \tau^- + \text{jets}$.

TABLE IV. Reconstruction and cut conditions in the ATLAS soft-leptons + jets + \cancel{E}_T analysis at $\sqrt{s} = 13$ TeV [74].

Reconstruction conditions	
Electron $p_T, \eta $	$> 4.5 \text{ GeV}, < 2.47$
Muon $p_T, \eta $	$> 4 \text{ GeV}, < 2.5$
Non- b -tagged jet $p_T, \eta $	$> 30 \text{ GeV}, < 2.8$
b -tagged jet $p_T, \eta $	$> 20 \text{ GeV}, < 2.5$
Cut conditions	
Number of leptons	2
Lepton flavor and charge	e^+e^- or $\mu^+\mu^-$
Leading lepton $p_T^{\ell_1}$	$> 5 \text{ GeV}$
Subleading lepton $p_T^{\ell_2}$	> 4.5 (4) GeV for $\ell_2 = e$ (μ)
$\Delta R_{\ell\ell}$	$0.05 < \Delta R_{\ell\ell} < 2$
$m_{\ell\ell}$	$[1, 3] \cup [3.2, 60] \text{ GeV}$
\cancel{E}_T	$> 200 \text{ GeV}$
Number of jets	≥ 1
Leading jet p_T	$> 100 \text{ GeV}$
$\Delta\phi(j_1, \cancel{\mathbf{p}}_T)$	> 2
$\min(\Delta\phi(j_i, \cancel{\mathbf{p}}_T))$	> 0.4
Number of b -tagged jets	0
$m_{\tau\tau}$	< 0 or $> 160 \text{ GeV}$
$m_T^{\ell_1}$	$< 70 \text{ GeV}$
$\cancel{E}_T/H_T^{\text{lep}}$	$> \max(5, 15 - 2m_{\ell\ell}/\text{GeV})$

A. LHC constraint

We reinterpret the ATLAS analysis [74] to study the current constraint on the QSDM model in the soft-leptons + jets + \cancel{E}_T channel. The corresponding reconstruction and cut conditions are summarized in Table IV. The p_T thresholds for reconstructed electrons and muons are lowered to 4.5 and 4 GeV for keeping soft leptons in the final state. There should be exact two leptons forming a SFOS pair, whose direction distance $\Delta R_{\ell\ell}$ and invariant mass $m_{\ell\ell}$ should lie in proper ranges because they are considered to be originated from an off-shell Z boson. Events with $m_{\ell\ell} \in (3, 3.2) \text{ GeV}$ are rejected to avoid contamination from J/ψ decays. In order to increase the signal-to-background ratio, at least one jet with $p_T > 100 \text{ GeV}$ and $\cancel{E}_T > 200 \text{ GeV}$ are required. The condition $\Delta\phi(j_1, \cancel{\mathbf{p}}_T) > 2$ is used to ensure the transverse directions of the leading jet and $\cancel{\mathbf{p}}_T$ are quite opposite. In order to suppress the $t\bar{t}$ + jets and tW + jets backgrounds, no b -tagged jet is allowed.

For further increasing the signal significance, some dedicated kinematic variables are utilized. The $m_{\tau\tau}$ variable [53, 54, 74, 75] constructed by the SFOS lepton pair is help-

TABLE V. Signal regions defined by the $m_{\ell\ell}$ bins in the ATLAS soft-leptons + jets + \cancel{E}_T analysis at $\sqrt{s} = 13$ TeV [74].

Signal regions	SR1	SR2	SR3	SR4	SR5	SR6	SR7
$m_{\ell\ell}$ (GeV)	[1,3]	[1,5]	[1,10]	[1,20]	[1,30]	[1,40]	[1,60]
$\sigma_{\text{vis}}^{\text{obs}}$ (fb)	0.10	0.18	0.34	0.61	0.59	0.72	0.80

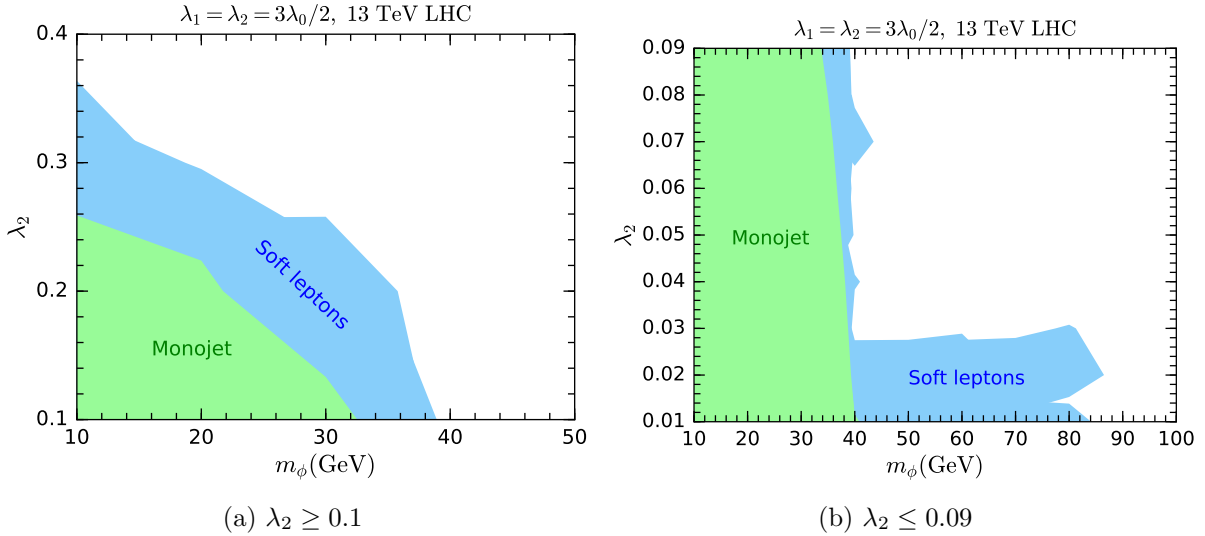


FIG. 6. Constraints from current LHC searches in the m_ϕ - λ_2 plane with the fixed coupling relation $\lambda_1 = \lambda_2 = 3\lambda_0/2$ for $\lambda_2 \geq 0.1$ (a) and $\lambda_2 \leq 0.09$ (b). Blue (green) regions are excluded at 95% C.L. by the ATLAS soft-leptons + jets + \cancel{E}_T [74] (monojet + \cancel{E}_T [69]) analysis at the 13 TeV LHC with a dataset of 36.1 fb^{-1} .

ful for reducing the $\tau^+\tau^- + \text{jets}$ background. The leading lepton transverse mass $m_T^{\ell_1} = \sqrt{2(E_T^{\ell_1} \cancel{E}_T - \mathbf{p}_T^{\ell_1} \cdot \mathbf{p}_T)}$ is required to satisfy $m_T^{\ell_1} < 70 \text{ GeV}$, in order to suppress the $t\bar{t} + \text{jets}$, $VV + \text{jets}$, and $W + \text{jets}$ backgrounds. The ratio of \cancel{E}_T to the scalar sum of the transverse momenta of the leptons $H_T^{\text{lep}} = p_T^{\ell_1} + p_T^{\ell_2}$ is used to improve the signal-to-background discrimination for compressed spectra.

We find that seven signal regions in the ATLAS analysis [74] could be sensitive to the QSDM model. They are defined with different inclusive $m_{\ell\ell}$ bins, as tabulated in Table V. Note that the (3, 3.2) GeV interval has also removed in these bins. We also list the corresponding 95% C.L. observed limits on the visible cross section, $\sigma_{\text{vis}}^{\text{obs}}$. We thus simulate signal samples and apply the above cuts to obtain 95% C.L. exclusion limits on the QSDM model.

The exclusion regions from the seven signal regions are combined, shown as the blue regions in Fig. 6. The fixed coupling relation in Figs. 6(a) and 6(b) is identical to that in Fig. 5(a). For comparison, we also demonstrate the green regions excluded by the ATLAS monojet search, which has been discussed in the previous section. We find that the soft-leptons + jets + \cancel{E}_T channel is more sensitive than the monojet + \cancel{E}_T channel at

TABLE VI. Information of the four benchmark points with the fixed coupling relation $\lambda_1 = \lambda_2 = 3\lambda_0/2$ for the soft-leptons + jets + \cancel{E}_T channel.

	M_X/GeV	λ_2	m_{++}/GeV	m_ϕ/GeV	m_a/GeV	m_1/GeV	m_2/GeV
BMP1	400	0.2	405.0	400	419.7	401.0	418.7
BMP2	400	0.4	410.0	400	438.5	402.0	436.7
BMP3	500	0.2	504.0	500	515.9	500.8	515.1
BMP4	200	0.4	219.2	200	268.8	203.9	265.9

$\sqrt{s} = 13$ TeV. In Fig. 6(a) for $\lambda_2 \geq 0.1$, the soft-lepton search has excluded a region with $m_\phi \lesssim 39$ GeV. In Fig. 6(b), we focus on the small λ_2 region ($\lambda_2 \leq 0.09$) and find that the soft-lepton search can probe up to $m_\phi \sim 85$ GeV for $\lambda_2 \lesssim 0.03$. The reason is that the $\cancel{E}_T/H_T^{\text{lep}}$ cut is more suitable for small mass splittings, say, $m_a - m_\phi \lesssim 20$ GeV, which is realized in such a $\lambda_2 \lesssim 0.03$ region.

B. Sensitivity at a 100 TeV pp collider

In this subsection, we explore the soft-leptons+jets+ \cancel{E}_T channel at a 100 TeV pp collider. The main backgrounds $t\bar{t}$ +jets, tW +jets, VV +jets, and $\tau^+\tau^-$ +jets are taken into account. In order to demonstrate a detailed study, we choose four BMPs for this channel with the fixed coupling relation $\lambda_1 = \lambda_2 = 3\lambda_0/2$, which leads to $\lambda_{h\phi\phi} = 0$ and $m_\phi = m_X$. The parameters and mass spectra of the BMPs are displayed in Table VI. These BMPs would not be constrained by direct detection experiments, and they predict DM relic abundance lower than the observation. BMP1 and BMP2 have identical M_X and different λ_2 , and, thus, a large λ_2 leads to larger mass splittings. If λ_2 is fixed, a larger M_X gives smaller mass splittings. This can be seen by comparing BMP3 to BMP1 or BMP4 to BMP2.

For a pp collider at $\sqrt{s} = 100$ TeV, we adopt the following reconstruction conditions with higher p_T thresholds than those used at the LHC.

- Reconstructed electrons are required to have $p_T > 10$ GeV and $|\eta| < 2.47$.
- Reconstructed muons are required to have $p_T > 10$ GeV and $|\eta| < 2.5$.
- Reconstructed non- b -tagged jets are required to have $p_T > 60$ GeV and $|\eta| < 2.8$.
- Reconstructed b -tagged jets are required to have $p_T > 40$ GeV and $|\eta| < 2.5$.

We appropriately modify the cut conditions according to a collision energy of 100 TeV. They are classified into six subsequent cuts, as tabulated in Table VII. The $m_T^{\ell_1}$ cut is abandoned, as we find that it would not be helpful.

Cut 1 selects the events with a proper soft SFOS lepton pair. After applying cut 1, the fraction of events binned in the leading jet p_T for the four BMPs and for the backgrounds

TABLE VII. Cut conditions in the soft-leptons + jets + \cancel{E}_T channel at a 100 TeV pp collider.

Cut 1	Exact two SFOS leptons
	Leading lepton $p_T > 12$ GeV, $0.05 < \Delta R_{\ell\ell} < 2$
Cut 2	At least one jet, no b -tagged jet
	Leading jet $p_T > 200$ GeV
	$\Delta\phi(j_1, \cancel{p}_T) > 2.0$, $\min(\Delta\phi(j_i, \cancel{p}_T)) > 0.4$
Cut 3	$m_{\tau\tau} < 0$ or $m_{\tau\tau} > 200$ GeV
Cut 4	$\cancel{E}_T > 280$ GeV
Cut 5	$\cancel{E}_T/H_T^{\text{lep}} > \max(5, 15 - 2m_{\ell\ell}/\text{GeV})$
Cut 6	$m_{\ell\ell} \in [1, 3] \cup [3.2, 60]$ GeV

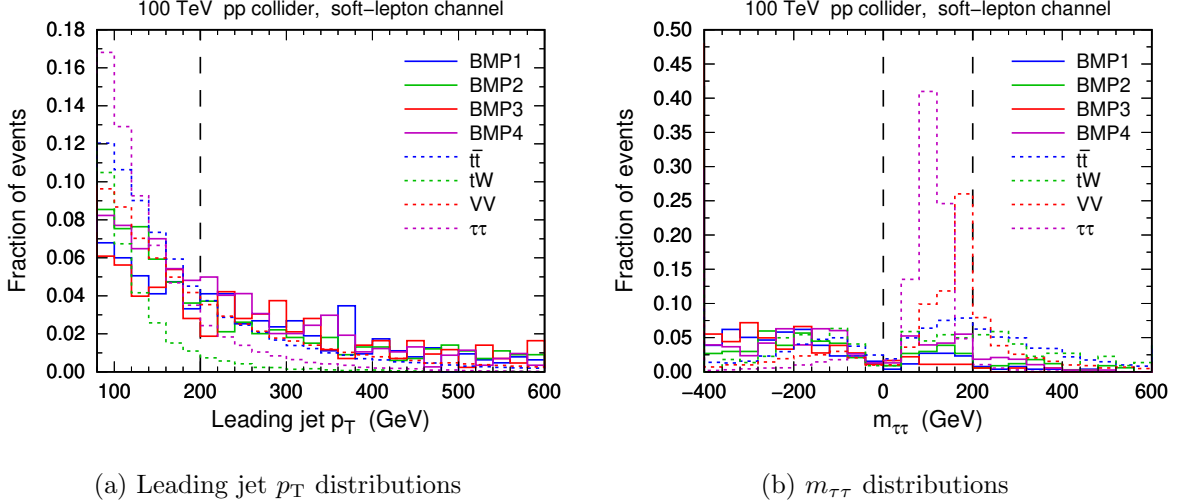


FIG. 7. Fraction of signal and background events binned in the leading jet p_T after cut 1 (a) and in $m_{\tau\tau}$ after cut 2 (b) in the soft-leptons + jets + \cancel{E}_T channel at a 100 TeV pp collider. Dashed lines indicate the cut thresholds.

$t\bar{t}$ + jets, tW + jets, VV + jets, and $\tau^+\tau^-$ + jets are presented in Fig. 7(a). We can see that these backgrounds tend to have lower p_T . Thus, we require the leading jet $p_T > 200$ GeV in cut 2 for reducing the backgrounds.

Figure 7(b) shows the $m_{\tau\tau}$ distributions of signal and background events after cut 2. The $m_{\tau\tau}$ variable is defined by $m_{\tau\tau} = \text{sgn}(m_{\tau\tau}^2)\sqrt{|m_{\tau\tau}^2|}$ with $m_{\tau\tau}^2 \equiv (1 + \xi_1)(1 + \xi_2)m_{\ell\ell}^2$, where ξ_1 and ξ_2 are parameters determined by solving $\cancel{p}_T = \xi_1\mathbf{p}_T^{\ell_1} + \xi_2\mathbf{p}_T^{\ell_2}$ event by event [53, 54, 74, 75]. If the τ leptons in the $pp \rightarrow Z^{(*)}/\gamma^*(\rightarrow \tau^+\tau^-)$ + jets process both decay leptonically and the daughter neutrinos are collinear with the daughter charged leptons, such a $m_{\tau\tau}$ definition will truly correspond to the invariant mass of the τ leptons when the missing transverse momentum \cancel{p}_T is genuinely contributed by the neutrinos. Such a collinear situation would be

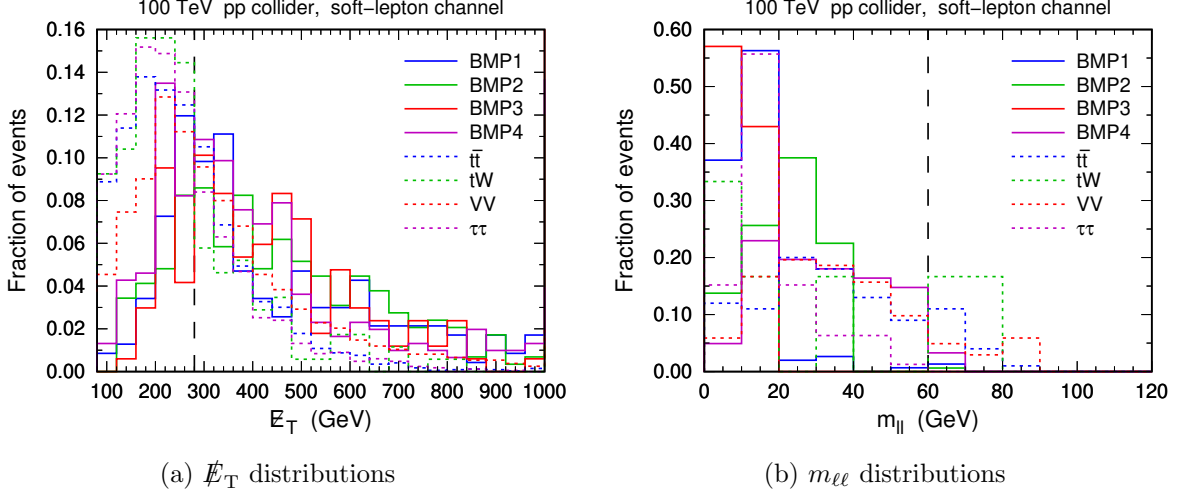


FIG. 8. Fraction of signal and background events binned in E_T after cut 3 (a) and in $m_{\ell\ell}$ after cut 5 (b) in the soft-leptons + jets + E_T channel at a 100 TeV pp collider. Dashed lines indicate the cut thresholds.

realized when the two τ leptons are sufficiently boosted. Consequently, the $m_{\tau\tau}$ distribution of the $\tau^+\tau^- + \text{jets}$ background peaks around m_Z , as demonstrated in Fig. 7(b). Additionally, the $VV + \text{jets}$ distribution peaks around $2m_W$ because of the $W^+W^- \rightarrow \tau^+\tau^-\nu_\tau\bar{\nu}_\tau$ decay process. Therefore, a veto on the events with $m_{\tau\tau} \in [0, 200]$ GeV in cut 3 can significantly suppress the $\tau^+\tau^- + \text{jets}$ and $VV + \text{jets}$ backgrounds.

Figure 8(a) presents the E_T distributions after applying cut 3. We find that the signal distributions are typically harder than the backgrounds, because the DM candidate ϕ with a mass of $\mathcal{O}(10^2)$ GeV induces larger E_T than neutrinos. Thus, we adopt the condition $E_T > 280$ GeV in cut 4 to increase the signal significance. Cut 5 and cut 6 make use of the E_T/H_T^{lep} and $m_{\ell\ell}$ variables, following the ATLAS analysis [74].

The $m_{\ell\ell}$ distributions after applying cut 5 are displayed in Fig. 8(b). Inferring from Table VI, we have $m_a - m_\phi \sim 20, 39, 16$, and 69 GeV for BMP1, BMP2, BMP3, and BMP4, respectively. Such a difference in the mass splitting results in different end points in the $m_{\ell\ell}$ distributions, as clearly shown in Fig. 8(b). Seven signal regions are defined by the $m_{\ell\ell}$ bins as the same as those in Table V. Different $m_{\ell\ell}$ bins would be suitable for different mass splittings.

Table VIII lists the visible cross section and the signal significance for an integrated luminosity of 3 ab^{-1} after applying each cut in SR3. We can see that the signal significances of the four BMPs subsequently increase from cut 1 to cut 5. The cut condition $m_{\ell\ell} \in [1, 3] \cup [3.2, 10]$ GeV in SR3 increases the significances of BMP1 and BMP3 but decreases those of BMP2 and BMP4. This is because BMP1 and BMP3 have smaller mass splittings and, hence, sufficient fractions of events satisfying $m_{\ell\ell} \leq 10$ GeV, while BMP2 and BMP4 do not, as shown in Fig. 8(b). Larger $m_{\ell\ell}$ bins in SR6 and SR7 would be applicable for BMP2 and BMP4.

TABLE VIII. Visible cross section σ_{vis} in femtobarns and signal significance \mathcal{S} for integrated luminosity 3 ab^{-1} after each cut in SR3 of the soft-leptons + jets + \cancel{E}_T channel at $\sqrt{s} = 100 \text{ TeV}$.

	$t\bar{t}$	tW	VV	$\tau\tau$	BMP1		BMP2		BMP3		BMP4	
	σ_{vis}	σ_{vis}	σ_{vis}	σ_{vis}	σ_{vis}	\mathcal{S}	σ_{vis}	\mathcal{S}	σ_{vis}	\mathcal{S}	σ_{vis}	\mathcal{S}
Cut 1	37600	28400	5070	5420	1.53	0.303	2.29	0.453	0.618	0.122	17.3	3.43
Cut 2	1790	296	804	510	0.625	0.586	0.770	0.722	0.262	0.246	5.77	5.42
Cut 3	1280	232	383	73.3	0.567	0.699	0.669	0.825	0.243	0.300	4.61	5.68
Cut 4	445	69.7	190	21.7	0.426	0.863	0.531	1.08	0.201	0.408	3.14	6.35
Cut 5	37.3	8.04	9.91	3.47	0.366	2.57	0.368	2.59	0.185	1.30	0.934	6.50
SR3	4.11	2.68	0.583	0.528	0.136	2.59	0.0483	0.921	0.106	2.02	0.0455	0.868

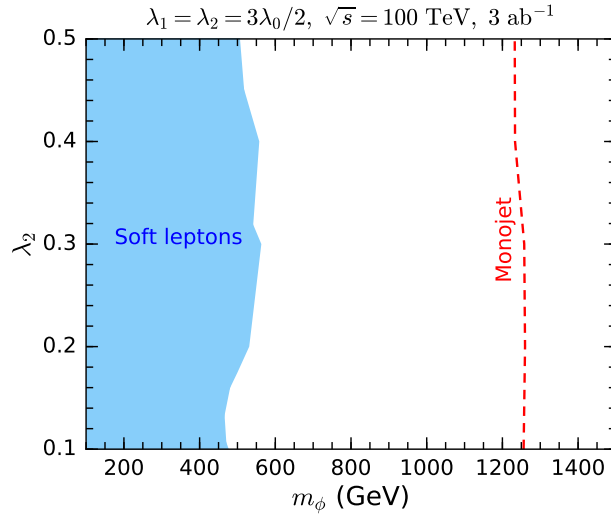


FIG. 9. 95% C.L. expected exclusion region in the soft-leptons + jets + \cancel{E}_T channel at a 100 TeV pp collider with an integrated luminosity of 3 ab^{-1} for the fixed coupling relation $\lambda_1 = \lambda_2 = 3\lambda_0/2$. For comparison, the red dashed line denotes the 95% C.L. expected exclusion limit in the monojet + \cancel{E}_T channel with the same collision energy and integrated luminosity.

Figure 9 shows the 95% C.L. expected exclusion region combining the seven signal regions at a 100 TeV pp collider with a dataset of 3 ab^{-1} for the fixed coupling relation $\lambda_1 = \lambda_2 = 3\lambda_0/2$. We find that the soft-leptons + jets + \cancel{E}_T channel can explore a region up to $m_\phi \sim 550 \text{ GeV}$. Nonetheless, such a sensitivity is not better than that in the monojet + \cancel{E}_T channel, which is demonstrated by the red dashed line.

VI. CONCLUSIONS AND DISCUSSIONS

In this paper, we discuss the QSDM model, where the dark sector contains an inert $\text{SU}(2)_L$ quadruplet scalar with $Y = 1/2$. After the electroweak symmetry breaking, there are one doubly charged scalar, two singly charged scalars, and two neutral scalars. For

$\lambda_2 > 0$, the lighter neutral scalar ϕ plays the role of DM particle. We have identified the parameter regions that can predict an observed DM relic abundance.

As the DM candidate can interact with nucleons through the SM Higgs portal, direct detection experiments could be sensitive to this model. We have investigated the constraints from the current experiment XENON1T as well as the sensitivity of the future LZ experiment. Nonetheless, the $h\phi\phi$ coupling could vanish if the quartic couplings λ_0 , λ_1 , and λ_2 satisfy special relations, resulting in null signal in direct detection. In this case, other types of DM search experiments would be essentially important.

Since the dark sector scalars carry electroweak charges, they could be directly produced in pairs at high-energy pp colliders. The mass splittings among the dark sector scalars are typically lower than m_W and m_Z . As a result, the sensitive search channels at the LHC include the monojet + \cancel{E}_T and soft-leptons + jets + \cancel{E}_T channels. We have recast the ATLAS analyses in these two channels with $\sqrt{s} = 13$ TeV and an integrated luminosity of 36.1 fb^{-1} . We have found that the monojet search has excluded some parameter regions up to $m_\phi \sim 45$ GeV, while the soft-lepton channel has excluded larger regions up to $m_\phi \sim 85$ GeV.

As these LHC constraints on the QSDM model still seem rather weak, we have studied the prospect of a future 100 TeV pp collider, either SPPC or FCC-hh. We have found that the monojet channel could be sensitive to the model up to $m_\phi \sim 1.2$ TeV assuming an integrated luminosity of 3 ab^{-1} . On the other hand, the soft-lepton channel is less sensitive, reaching up to $m_\phi \sim 550$ GeV.

Electroweak precision measurements provide an indirect probe to the QSDM model. The future determination of electroweak oblique parameters in the CEPC project would be able to reach up to $m_\phi \sim 0.6\text{--}1.3$ TeV. But a direct search in the monojet channel at a 100 TeV pp collider seems more sensitive in most regions.

Compared to the IDM, the QSDM model involves more electroweakly interacting dark sector scalars living in a larger $\text{SU}(2)_L$ representation. This effectively enhances the annihilation and coannihilation cross sections of the scalars in the early Universe. As a result, higher mass scales ($\gtrsim 2\text{--}3$ TeV) are required to yield the observed DM relic abundance. Another consequence is that the pair production rates of the scalars at pp colliders significantly increase. Therefore, the LHC and a 100 TeV pp collider are able to probe higher mass scales in the QSDM model than in the IDM (cf. Refs. [59, 76–78]).

ACKNOWLEDGMENTS

This work is supported in part by the National Natural Science Foundation of China under Grants No. 11805288, No. 11875327, and No. 11905300, the China Postdoctoral Science Foundation under Grant No. 2018M643282, the Natural Science Foundation of Guangdong Province under Grant No. 2016A030313313, the Fundamental Research Funds for the Central Universities, and the Sun Yat-Sen University Science Foundation.

Appendix A: Electroweak gauge interactions of the quadruplet scalar

The generators in the $SU(2)_L$ representation **4** are given by

$$T^1 = \begin{pmatrix} & \sqrt{3}/2 & & \\ \sqrt{3}/2 & & 1 & \\ & 1 & & \sqrt{3}/2 \\ & & \sqrt{3}/2 & \end{pmatrix}, \quad T^2 = \begin{pmatrix} & -\sqrt{3}i/2 & & \\ \sqrt{3}i/2 & & -i & \\ & i & & -\sqrt{3}i/2 \\ & & \sqrt{3}i/2 & \end{pmatrix},$$

$$T^3 = \text{diag} \left(\frac{3}{2}, \frac{1}{2}, -\frac{1}{2}, -\frac{3}{2} \right). \quad (\text{A1})$$

Utilizing these generators, we can expand the gauge interaction terms for the quadruplet scalar as

$$\begin{aligned} \mathcal{L}_{\text{gauge}} = & g \left[\frac{\sqrt{6}}{2} W_\mu^+ (X^{++})^* i \overleftrightarrow{\partial}^\mu X^+ + \sqrt{2} W_\mu^+ (X^+)^* i \overleftrightarrow{\partial}^\mu X^0 + \frac{\sqrt{6}}{2} W_\mu^+ (X^0)^* i \overleftrightarrow{\partial}^\mu X^- + \text{H.c.} \right] \\ & + e A_\mu \left[2(X^{++})^* i \overleftrightarrow{\partial}^\mu X^{++} + (X^+)^* i \overleftrightarrow{\partial}^\mu X^+ - (X^-)^* i \overleftrightarrow{\partial}^\mu X^- \right] \\ & + \frac{g}{2c_W} Z_\mu \left[(3c_W^2 - s_W^2)(X^{++})^* i \overleftrightarrow{\partial}^\mu X^{++} + (c_W^2 - s_W^2)(X^+)^* i \overleftrightarrow{\partial}^\mu X^+ \right. \\ & \quad \left. + i a i \overleftrightarrow{\partial}^\mu \phi - (3c_W^2 + s_W^2)(X^-)^* i \overleftrightarrow{\partial}^\mu X^- \right] \\ & + \frac{g^2}{2} W_\mu^+ W^{-\mu} [3|X^{++}|^2 + 7|X^+|^2 + 7|X^0|^2 + 3|X^-|^2] \\ & + g^2 \left[\sqrt{3} W_\mu^+ W^{+\mu} (X^{++})^* X^0 + \sqrt{3} W_\mu^+ W^{+\mu} (X^+)^* X^- + \text{H.c.} \right] \\ & + e^2 A_\mu A^\mu (4|X^{++}|^2 + |X^+|^2 + |X^-|^2) \\ & + \frac{eg}{c_W} A_\mu Z^\mu [2(3c_W^2 - s_W^2)|X^{++}|^2 + (c_W^2 - s_W^2)|X^+|^2 + (3c_W^2 + s_W^2)|X^-|^2] \\ & + \frac{g^2}{4c_W^2} Z_\mu Z^\mu [(3c_W^2 - s_W^2)^2 |X^{++}|^2 + (c_W^2 - s_W^2)^2 |X^+|^2 + |X^0|^2 + (3c_W^2 + s_W^2)^2 |X^-|^2] \\ & + \left\{ \left[\frac{3\sqrt{6}}{2} eg A^\mu + \frac{\sqrt{6}g^2(2c_W^2 - s_W^2)}{2c_W} Z^\mu \right] W_\mu^+ (X^{++})^* X^+ \right. \\ & \quad + \left(\sqrt{2} eg A^\mu - \frac{\sqrt{2}g^2 s_W^2}{c_W} Z^\mu \right) W_\mu^+ (X^+)^* X^0 \\ & \quad \left. - \left[\frac{\sqrt{6}}{2} eg A^\mu + \frac{\sqrt{6}g^2(2c_W^2 + s_W^2)}{2c_W} Z^\mu \right] W_\mu^+ (X^0)^* X^- + \text{H.c.} \right\}. \quad (\text{A2}) \end{aligned}$$

Here $c_W \equiv \cos \theta_W$ and $s_W \equiv \sin \theta_W$, where $\theta_W = \tan^{-1}(g'/g)$ is the weak mixing angle.

-
- [1] G. Bertone, D. Hooper, and J. Silk, “Particle dark matter: Evidence, candidates and constraints,” *Phys. Rept.* **405** (2005) 279–390, [arXiv:hep-ph/0404175 \[hep-ph\]](#).
 - [2] J. L. Feng, “Dark Matter Candidates from Particle Physics and Methods of Detection,” *Ann. Rev. Astron. Astrophys.* **48** (2010) 495–545, [arXiv:1003.0904 \[astro-ph.CO\]](#).
 - [3] B.-L. Young, “A survey of dark matter and related topics in cosmology,” *Front. Phys.(Beijing)* **12** (2017) 121201. [Erratum: *Front. Phys.(Beijing)*12,no.2,121202(2017)].
 - [4] R. Mahbubani and L. Senatore, “The Minimal model for dark matter and unification,” *Phys. Rev.* **D73** (2006) 043510, [arXiv:hep-ph/0510064 \[hep-ph\]](#).
 - [5] M. Cirelli, N. Fornengo, and A. Strumia, “Minimal dark matter,” *Nucl. Phys.* **B753** (2006) 178–194, [arXiv:hep-ph/0512090 \[hep-ph\]](#).
 - [6] T. Hambye, F. S. Ling, L. Lopez Honorez, and J. Rocher, “Scalar Multiplet Dark Matter,” *JHEP* **07** (2009) 090, [arXiv:0903.4010 \[hep-ph\]](#). [Erratum: *JHEP*05,066(2010)].
 - [7] T. Cohen, J. Kearney, A. Pierce, and D. Tucker-Smith, “Singlet-Doublet Dark Matter,” *Phys. Rev.* **D85** (2012) 075003, [arXiv:1109.2604 \[hep-ph\]](#).
 - [8] Y. Cai, W. Chao, and S. Yang, “Scalar Septuplet Dark Matter and Enhanced $h \rightarrow \gamma\gamma$ Decay Rate,” *JHEP* **12** (2012) 043, [arXiv:1208.3949 \[hep-ph\]](#).
 - [9] K. Earl, K. Hartling, H. E. Logan, and T. Pilkington, “Constraining models with a large scalar multiplet,” *Phys. Rev.* **D88** (2013) 015002, [arXiv:1303.1244 \[hep-ph\]](#).
 - [10] S. S. AbdusSalam and T. A. Chowdhury, “Scalar Representations in the Light of Electroweak Phase Transition and Cold Dark Matter Phenomenology,” *JCAP* **1405** (2014) 026, [arXiv:1310.8152 \[hep-ph\]](#).
 - [11] O. Fischer and J. J. van der Bij, “The scalar Singlet-Triplet Dark Matter Model,” *JCAP* **1401** (2014) 032, [arXiv:1311.1077 \[hep-ph\]](#).
 - [12] A. Dedes and D. Karamitros, “Doublet-Triplet Fermionic Dark Matter,” *Phys. Rev.* **D89** (2014) 115002, [arXiv:1403.7744 \[hep-ph\]](#).
 - [13] B. Ostdiek, “Constraining the minimal dark matter fiveplet with LHC searches,” *Phys. Rev.* **D92** (2015) 055008, [arXiv:1506.03445 \[hep-ph\]](#).
 - [14] C. Cai, Z.-M. Huang, Z. Kang, Z.-H. Yu, and H.-H. Zhang, “Perturbativity Limits for Scalar Minimal Dark Matter with Yukawa Interactions: Septuplet,” *Phys. Rev.* **D92** (2015) 115004, [arXiv:1510.01559 \[hep-ph\]](#).
 - [15] T. M. P. Tait and Z.-H. Yu, “Triplet-Quadruplet Dark Matter,” *JHEP* **03** (2016) 204, [arXiv:1601.01354 \[hep-ph\]](#).
 - [16] S. Banerjee, S. Matsumoto, K. Mukaida, and Y.-L. S. Tsai, “WIMP Dark Matter in a Well-Tempered Regime: A case study on Singlet-Doublets Fermionic WIMP,” *JHEP* **11** (2016) 070, [arXiv:1603.07387 \[hep-ph\]](#).

- [17] W.-B. Lu and P.-H. Gu, “Mixed Inert Scalar Triplet Dark Matter, Radiative Neutrino Masses and Leptogenesis,” *Nucl. Phys.* **B924** (2017) 279–311, [arXiv:1611.02106 \[hep-ph\]](#).
- [18] C. Cai, Z.-H. Yu, and H.-H. Zhang, “CEPC Precision of Electroweak Oblique Parameters and Weakly Interacting Dark Matter: the Fermionic Case,” *Nucl. Phys.* **B921** (2017) 181–210, [arXiv:1611.02186 \[hep-ph\]](#).
- [19] C. Cai, Z.-H. Yu, and H.-H. Zhang, “CEPC Precision of Electroweak Oblique Parameters and Weakly Interacting Dark Matter: the Scalar Case,” *Nucl. Phys.* **B924** (2017) 128–152, [arXiv:1705.07921 \[hep-ph\]](#).
- [20] X. Liu and L. Bian, “Dark matter and electroweak phase transition in the mixed scalar dark matter model,” *Phys. Rev.* **D97** (2018) 055028, [arXiv:1706.06042 \[hep-ph\]](#).
- [21] Q.-F. Xiang, X.-J. Bi, P.-F. Yin, and Z.-H. Yu, “Exploring Fermionic Dark Matter via Higgs Boson Precision Measurements at the Circular Electron Positron Collider,” *Phys. Rev.* **D97** (2018) 055004, [arXiv:1707.03094 \[hep-ph\]](#).
- [22] C. Cai, Z. Kang, Z. Luo, Z.-H. Yu, and H.-H. Zhang, “Scalar quintuplet minimal dark matter with Yukawa interactions: perturbative up to the Planck scale,” *Chin. Phys.* **C43** (2019) 023102, [arXiv:1711.07396 \[hep-ph\]](#).
- [23] L. Lopez Honorez, M. H. G. Tytgat, P. Tziveloglou, and B. Zaldivar, “On Minimal Dark Matter coupled to the Higgs,” *JHEP* **04** (2018) 011, [arXiv:1711.08619 \[hep-ph\]](#).
- [24] C. Cai, Z. Kang, H.-H. Zhang, and Y.-P. Zeng, “Minimal dark matter in $SU(2)_L \times U(1)_Y \times U(1)_{B-L}$,” *Phys. Lett.* **B784** (2018) 385–391, [arXiv:1801.05594 \[hep-ph\]](#).
- [25] A. Dutta Banik, A. K. Saha, and A. Sil, “Scalar assisted singlet doublet fermion dark matter model and electroweak vacuum stability,” *Phys. Rev.* **D98** (2018) 075013, [arXiv:1806.08080 \[hep-ph\]](#).
- [26] P.-H. Gu and H.-J. He, “TeV Scale Neutrino Mass Generation, Minimal Inelastic Dark Matter, and High Scale Leptogenesis,” *Phys. Rev.* **D99** (2019) 015025, [arXiv:1808.09377 \[hep-ph\]](#).
- [27] A. Betancur and Ó. Zapata, “Phenomenology of doublet-triplet fermionic dark matter in nonstandard cosmology and multicomponent dark sectors,” *Phys. Rev.* **D98** (2018) 095003, [arXiv:1809.04990 \[hep-ph\]](#).
- [28] K. Kadota and A. Spray, “Electroweak Multiplet Dark Matter at Future Lepton Colliders,” *JHEP* **02** (2019) 017, [arXiv:1811.00560 \[hep-ph\]](#).
- [29] J.-W. Wang, X.-J. Bi, P.-F. Yin, and Z.-H. Yu, “Impact of Fermionic Electroweak Multiplet Dark Matter on Vacuum Stability with One-loop Matching,” *Phys. Rev.* **D99** (2019) 055009, [arXiv:1811.08743 \[hep-ph\]](#).
- [30] A. Filimonova and S. Westhoff, “Long live the Higgs portal!,” *JHEP* **02** (2019) 140, [arXiv:1812.04628 \[hep-ph\]](#).

- [31] W. Chao, G.-J. Ding, X.-G. He, and M. Ramsey-Musolf, “Scalar Electroweak Multiplet Dark Matter,” *JHEP* **08** (2019) 058, [arXiv:1812.07829 \[hep-ph\]](#).
- [32] T. Abe and R. Sato, “Current status and future prospects of the singlet-doublet dark matter model with CP-violation,” *Phys. Rev.* **D99** (2019) 035012, [arXiv:1901.02278 \[hep-ph\]](#).
- [33] Y. Cheng and W. Liao, “Fate of false vacuum in a singlet-doublet dark matter model with RG improved effective action,” [arXiv:1909.11941 \[hep-ph\]](#).
- [34] N. G. Deshpande and E. Ma, “Pattern of Symmetry Breaking with Two Higgs Doublets,” *Phys. Rev.* **D18** (1978) 2574.
- [35] R. Barbieri, L. J. Hall, and V. S. Rychkov, “Improved naturalness with a heavy Higgs: An Alternative road to LHC physics,” *Phys. Rev.* **D74** (2006) 015007, [arXiv:hep-ph/0603188 \[hep-ph\]](#).
- [36] M. Gustafsson, E. Lundstrom, L. Bergstrom, and J. Edsjo, “Significant Gamma Lines from Inert Higgs Dark Matter,” *Phys. Rev. Lett.* **99** (2007) 041301, [arXiv:astro-ph/0703512 \[ASTRO-PH\]](#).
- [37] Q.-H. Cao, E. Ma, and G. Rajasekaran, “Observing the Dark Scalar Doublet and its Impact on the Standard-Model Higgs Boson at Colliders,” *Phys. Rev.* **D76** (2007) 095011, [arXiv:0708.2939 \[hep-ph\]](#).
- [38] P. Fileviez Perez, H. H. Patel, M. Ramsey-Musolf, and K. Wang, “Triplet Scalars and Dark Matter at the LHC,” *Phys. Rev.* **D79** (2009) 055024, [arXiv:0811.3957 \[hep-ph\]](#).
- [39] T. Araki, C. Q. Geng, and K. I. Nagao, “Dark Matter in Inert Triplet Models,” *Phys. Rev.* **D83** (2011) 075014, [arXiv:1102.4906 \[hep-ph\]](#).
- [40] F.-X. Josse-Michaux and E. Molinaro, “Triplet scalar dark matter and leptogenesis in an inverse seesaw model of neutrino mass generation,” *Phys. Rev.* **D87** (2013) 036007, [arXiv:1210.7202 \[hep-ph\]](#).
- [41] S. Yaser Ayazi and S. M. Firouzabadi, “Constraining Inert Triplet Dark Matter by the LHC and FermiLAT,” *JCAP* **1411** (2014) 005, [arXiv:1408.0654 \[hep-ph\]](#).
- [42] N. Khan, “Exploring the hyperchargeless Higgs triplet model up to the Planck scale,” *Eur. Phys. J.* **C78** (2018) 341, [arXiv:1610.03178 \[hep-ph\]](#).
- [43] **CEPC Study Group** Collaboration, M. Dong *et al.*, “CEPC Conceptual Design Report: Volume 2 - Physics & Detector,” [arXiv:1811.10545 \[hep-ex\]](#).
- [44] M. Beltran, D. Hooper, E. W. Kolb, Z. A. C. Krusberg, and T. M. P. Tait, “Maverick dark matter at colliders,” *JHEP* **09** (2010) 037, [arXiv:1002.4137 \[hep-ph\]](#).
- [45] A. Rajaraman, W. Shepherd, T. M. P. Tait, and A. M. Wijangco, “LHC Bounds on Interactions of Dark Matter,” *Phys. Rev.* **D84** (2011) 095013, [arXiv:1108.1196 \[hep-ph\]](#).
- [46] P. J. Fox, R. Harnik, J. Kopp, and Y. Tsai, “Missing Energy Signatures of Dark Matter at the LHC,” *Phys. Rev.* **D85** (2012) 056011, [arXiv:1109.4398 \[hep-ph\]](#).
- [47] Z.-H. Yu, X.-J. Bi, Q.-S. Yan, and P.-F. Yin, “Detecting light stop pairs in coannihilation scenarios at the LHC,” *Phys. Rev.* **D87** (2013) 055007, [arXiv:1211.2997 \[hep-ph\]](#).

- [48] Q.-F. Xiang, X.-J. Bi, P.-F. Yin, and Z.-H. Yu, “Searches for dark matter signals in simplified models at future hadron colliders,” *Phys. Rev.* **D91** (2015) 095020, [arXiv:1503.02931 \[hep-ph\]](#).
- [49] J.-W. Wang, X.-J. Bi, Q.-F. Xiang, P.-F. Yin, and Z.-H. Yu, “Exploring triplet-quadruplet fermionic dark matter at the LHC and future colliders,” *Phys. Rev.* **D97** (2018) 035021, [arXiv:1711.05622 \[hep-ph\]](#).
- [50] G. F. Giudice, T. Han, K. Wang, and L.-T. Wang, “Nearly Degenerate Gauginos and Dark Matter at the LHC,” *Phys. Rev.* **D81** (2010) 115011, [arXiv:1004.4902 \[hep-ph\]](#).
- [51] S. Gori, S. Jung, and L.-T. Wang, “Cornering electroweakinos at the LHC,” *JHEP* **10** (2013) 191, [arXiv:1307.5952 \[hep-ph\]](#).
- [52] P. Schwaller and J. Zurita, “Compressed electroweakino spectra at the LHC,” *JHEP* **03** (2014) 060, [arXiv:1312.7350 \[hep-ph\]](#).
- [53] Z. Han, G. D. Kribs, A. Martin, and A. Menon, “Hunting quasidegenerate Higgsinos,” *Phys. Rev.* **D89** (2014) 075007, [arXiv:1401.1235 \[hep-ph\]](#).
- [54] H. Baer, A. Mustafayev, and X. Tata, “Monojet plus soft dilepton signal from light higgsino pair production at LHC14,” *Phys. Rev.* **D90** (2014) 115007, [arXiv:1409.7058 \[hep-ph\]](#).
- [55] **CEPC-SPPC Study Group** Collaboration, M. Ahmad *et al.*, “CEPC-SPPC Preliminary Conceptual Design Report. 1. Physics and Detector,” IHEP-CEPC-DR-2015-01, IHEP-TH-2015-01, IHEP-EP-2015-01.
- [56] **FCC** Collaboration, A. Abada *et al.*, “FCC Physics Opportunities,” *Eur. Phys. J.* **C79** (2019) 474.
- [57] Y. Hamada, K. Kawana, and K. Tsumura, “Landau pole in the Standard Model with weakly interacting scalar fields,” *Phys. Lett. B* **747** (2015) 238–244, [arXiv:1505.01721 \[hep-ph\]](#).
- [58] G. Degrandi, S. Di Vita, J. Elias-Miro, J. R. Espinosa, G. F. Giudice, G. Isidori, and A. Strumia, “Higgs mass and vacuum stability in the Standard Model at NNLO,” *JHEP* **08** (2012) 098, [arXiv:1205.6497 \[hep-ph\]](#).
- [59] A. Belyaev, G. Cacciapaglia, I. P. Ivanov, F. Rojas-Abatte, and M. Thomas, “Anatomy of the Inert Two Higgs Doublet Model in the light of the LHC and non-LHC Dark Matter Searches,” *Phys. Rev.* **D97** (2018) 035011, [arXiv:1612.00511 \[hep-ph\]](#).
- [60] K. Griest and D. Seckel, “Three exceptions in the calculation of relic abundances,” *Phys. Rev.* **D43** (1991) 3191–3203.
- [61] A. Alloul, N. D. Christensen, C. Degrande, C. Duhr, and B. Fuks, “FeynRules 2.0 - A complete toolbox for tree-level phenomenology,” *Comput. Phys. Commun.* **185** (2014) 2250–2300, [arXiv:1310.1921 \[hep-ph\]](#).
- [62] J. Alwall, R. Frederix, S. Frixione, V. Hirschi, F. Maltoni, O. Mattelaer, H. S. Shao, T. Stelzer, P. Torrielli, and M. Zaro, “The automated computation of tree-level and next-to-leading order differential cross sections, and their matching to parton shower simulations,” *JHEP* **07** (2014) 079, [arXiv:1405.0301 \[hep-ph\]](#).

- [63] F. Ambrogio, C. Arina, M. Backovic, J. Heisig, F. Maltoni, L. Mantani, O. Mattelaer, and G. Mohlabeng, “MadDM v.3.0: a Comprehensive Tool for Dark Matter Studies,” *Phys. Dark Univ.* **24** (2019) 100249, [arXiv:1804.00044 \[hep-ph\]](#).
- [64] **Planck** Collaboration, N. Aghanim *et al.*, “Planck 2018 results. VI. Cosmological parameters,” [arXiv:1807.06209 \[astro-ph.CO\]](#).
- [65] **XENON** Collaboration, E. Aprile *et al.*, “Dark Matter Search Results from a One Ton-Year Exposure of XENON1T,” *Phys. Rev. Lett.* **121** (2018) 111302, [arXiv:1805.12562 \[astro-ph.CO\]](#).
- [66] B. J. Mount *et al.*, “LUX-ZEPLIN (LZ) Technical Design Report,” [arXiv:1703.09144 \[physics.ins-det\]](#).
- [67] Z.-H. Yu, J.-M. Zheng, X.-J. Bi, Z. Li, D.-X. Yao, and H.-H. Zhang, “Constraining the interaction strength between dark matter and visible matter: II. scalar, vector and spin-3/2 dark matter,” *Nucl. Phys.* **B860** (2012) 115–151, [arXiv:1112.6052 \[hep-ph\]](#).
- [68] J. R. Ellis, A. Ferstl, and K. A. Olive, “Reevaluation of the elastic scattering of supersymmetric dark matter,” *Phys. Lett.* **B481** (2000) 304–314, [arXiv:hep-ph/0001005 \[hep-ph\]](#).
- [69] **ATLAS** Collaboration, M. Aaboud *et al.*, “Search for dark matter and other new phenomena in events with an energetic jet and large missing transverse momentum using the ATLAS detector,” *JHEP* **01** (2018) 126, [arXiv:1711.03301 \[hep-ex\]](#).
- [70] T. Sjöstrand, S. Ask, J. R. Christiansen, R. Corke, N. Desai, P. Ilten, S. Mrenna, S. Prestel, C. O. Rasmussen, and P. Z. Skands, “An Introduction to PYTHIA 8.2,” *Comput. Phys. Commun.* **191** (2015) 159–177, [arXiv:1410.3012 \[hep-ph\]](#).
- [71] M. L. Mangano, M. Moretti, F. Piccinini, and M. Treccani, “Matching matrix elements and shower evolution for top-quark production in hadronic collisions,” *JHEP* **01** (2007) 013, [arXiv:hep-ph/0611129 \[hep-ph\]](#).
- [72] **DELPHES 3** Collaboration, J. de Favereau, C. Delaere, P. Demin, A. Giammanco, V. Lemaître, A. Mertens, and M. Selvaggi, “DELPHES 3, A modular framework for fast simulation of a generic collider experiment,” *JHEP* **02** (2014) 057, [arXiv:1307.6346 \[hep-ex\]](#).
- [73] **ATLAS** Collaboration, M. Aaboud *et al.*, “Search for electroweak production of supersymmetric particles in final states with two or three leptons at $\sqrt{s} = 13$ TeV with the ATLAS detector,” *Eur. Phys. J.* **C78** (2018) 995, [arXiv:1803.02762 \[hep-ex\]](#).
- [74] **ATLAS** Collaboration, M. Aaboud *et al.*, “Search for electroweak production of supersymmetric states in scenarios with compressed mass spectra at $\sqrt{s} = 13$ TeV with the ATLAS detector,” *Phys. Rev.* **D97** (2018) 052010, [arXiv:1712.08119 \[hep-ex\]](#).
- [75] A. Barr and J. Scoville, “A boost for the EW SUSY hunt: monojet-like search for compressed sleptons at LHC14 with 100 fb^{-1} ,” *JHEP* **04** (2015) 147, [arXiv:1501.02511 \[hep-ph\]](#).

- [76] A. Arhrib, Y.-L. S. Tsai, Q. Yuan, and T.-C. Yuan, “An Updated Analysis of Inert Higgs Doublet Model in light of the Recent Results from LUX, PLANCK, AMS-02 and LHC,” *JCAP* **06** (2014) 030, [arXiv:1310.0358 \[hep-ph\]](#).
- [77] A. Datta, N. Ganguly, N. Khan, and S. Rakshit, “Exploring collider signatures of the inert Higgs doublet model,” *Phys. Rev. D* **95** (2017) 015017, [arXiv:1610.00648 \[hep-ph\]](#).
- [78] A. Belyaev, T. Fernandez Perez Tomei, P. Mercadante, C. Moon, S. Moretti, S. Novaes, L. Panizzi, F. Rojas, and M. Thomas, “Advancing LHC probes of dark matter from the inert two-Higgs-doublet model with the monojet signal,” *Phys. Rev. D* **99** (2019) 015011, [arXiv:1809.00933 \[hep-ph\]](#).